Journal of Materials Science: Materials in Electronics (2020) 31:5546–5553
https://doi.org/10.1007/s10854-020-03119-x

High energy storage efficiency and high electrostrictive coefficients in BNT–BS–*x*BT ferroelectric ceramics

Yabin Sun[1] · **Hua Wang**[1,2] · **Guobao Liu**[1] · **Hang Xie**[1] · **Changrong Zhou**[1,2] · **Guohua Chen**[1,2] · **Changlai Yuan**[1,2] · **Jiwen Xu**[1,2]

Received: 17 January 2020 / Accepted: 14 February 2020 / Published online: 24 February 2020

Abstract

$(1-x)[0.9(Bi_{0.5}Na_{0.5})TiO_3$–$0.1BiScO_3]$–$xBaTiO_3$ (BNT–BS–*x*BT) ceramics are prepared by the traditional solid-state sintering. The structure, morphology, ferroelectricity, strain, energy storage, dielectricity, and impedance of the BNT–BS–*x*BT ceramics are investigated. XRD shows that all ceramics have pseudo-cubic structures. The results also show that BT can refine the grain size of the ceramics and reduce the corresponding density. At $x=0.20$, the energy storage performance of the ceramics is optimum ($W_{rec}=0.563$ J/cm^3, $\eta=63\%$). At $x=0.10$, the electrostriction coefficient (Q_{33}) of the ceramics reaches 2.72325×10^{-2} m^4/C^2. Dielectric and impedance spectroscopies show that the ceramics are relaxor ferroelectrics and have good insulation properties.

1 Introduction

With the development of science and technology, traditional devices are developing towards miniaturization and multifunction, which needs materials with multiple properties at the same time. $PbZrTiO_3$ (PZT) is used in piezoelectric ceramic field owing to its excellent energy storage density ($W_{rec}=63.7$ J/cm^3) and efficiency ($\eta=81.3\%$) [1] and electrostrictive coefficient ($Q_{33}=0.033$–0.036 m^4/C^2) [2]. However, the volatilization of toxic PbO during high-temperature sintering not only causes environmental pollution but also generates instability in the composition and electrical properties of the products [3, 4]. Therefore, the development of lead-free piezoelectric materials has attracted much attention and many research programs for them have been carried out [5–9].

In 1961, Smolensky first synthesized $(Bi_{1-x}Na_x)TiO_3$ (BNT) lead-free ceramics, and they have attracted a lot of attentions due to its strong ferroelectricity ($P_r=38$ μC/cm^2), large piezoelectric coefficient ($K_{33}=40$–50%), and other advantages [10, 11]. However, it is difficult to be polarized because of its high coercive field ($E_c=73$ kV/cm); the high E_c also leads to large energy loss and affects energy storage performance. The defects make BNT ceramics difficult to replace Pb-based ceramics. Multi-component solid solution is one of the commonly used optimization methods for BNT ceramics. Some researchers have reported that the energy storage of BNT ceramics can be effectively improved by the method. For example, the introduction of $SrTiO_3$ and Sr $(Ti_{0.85}Zr_{0.15})$ O_3 into BNT ceramics can make the energy storage density of BNT ceramics reach 3.13 J/cm^3, and the energy storage efficiency is 91.14% [12]; The energy storage density of solid solution of BNT and $Ba_{0.94}La_{0.04}Zr_{0.02}Ti_{0.98}O_3$ under the action of $SrTiO_3$ and Li_2CO_3 is also as high as 2.72 J/cm^3 [13]. When $SrY_{0.5}Nb_{0.5}O_3$ is introduced into BNT-BT ceramics, the energy storage density of the ceramics is also 1.36 J/cm^3 [14]; In BNT–$SrTiO_3$ ceramics, the introduction of Bi $(Mg_{2/3}Nb_{1/3})O_3$ makes the energy storage density reach 3.45 J/cm^3 [15]. These results show that multi-component solid solution can effectively optimize the energy storage performance of BNT-based ceramics.

Electronic supplementary material The online version of this article (https://doi.org/10.1007/s10854-020-03119-x) contains supplementary material, which is available to authorized users.

✉ Hua Wang
wh65@tom.com

✉ Jiwen Xu
csuxjw@126.com

[1] School of Materials Science and Engineering, Guilin University of Electronic Technology, Guilin 541004, People's Republic of China

[2] Guangxi Key Laboratory of Information Materials, Guilin University of Electronic Technology, Guilin 541004, People's Republic of China

As for the electrostrictive properties of BNT-based ceramics, there are also many literature reports that $(1-x)$ $(Bi_{0.5}Na_{0.5})TiO_3$–$x$$BaTiO_3$ (BNT–BT) piezoelectric ceramics have morphotropic phase boundaries between the rhombohedral and tetragonal phases, where the piezoelectric property of BNT–BT ceramics is the best ($d_{33}=125$ pC/N), the E_c of the ceramics is also significantly reduced to 30 kV/cm, which makes the ceramics easier to polarize and reduces the energy loss in the energy storage [8, 9], and the electrostrictive coefficient (Q_{33}) of the ceramics also reached 0.022 m^4/C^2 [16]. Further, researchers found that adding $K_{0.5}Na_{0.5}NbO_3$ (KNN) or $SrTiO_3$ to BNT–BT ceramics can optimize the Q_{33} of the ceramics, the results showed that the Q_{33} of the ceramics all reached 0.026 m^4/C^2 [17, 18]. We have found that the $BiScO_3$ (BS) could improve the energy storage and the ferroelectric properties of BNT ceramics, in which the E_c of 0.9BNT–0.1BS ceramics can be effectively reduced to 15 kV/cm, and the energy storage density of the ceramics can reach 0.17 J/cm^3 [Details in the Supporting Information]. It also has been reported that BT can also optimize the Q_{33} of BNT ceramics reported in other works [16–18]. Therefore, we want to further optimize the BNT-based ceramics to have better energy storage and electrostrictive properties at the same time. This is a very interesting attempt; the 0.9BNT–0.1BS ceramic was selected as the matrix to investigate the effect of BT doping on the structure, surface morphology, and electrical properties of the 0.9BNT–0.1BS ceramics. The results indicated that the $(1-x)[0.9(Bi_{0.5}Na_{0.5})TiO_3–0.1BiScO_3]–xBaTiO_3$ (BNT–BS–xBT) ceramics can achieve an excellent energy storage efficiency ($\eta=63\%$) and a high electrostrictive coefficient ($Q_{33}=2.72325\times10^{-2}$ m^4/C^2).

2 Experimental

Six different compositions with $x=0.00$, 0.05, 0.10, 0.15, 0.20, and 0.25 in the BNT–BS–xBT ceramic system were designed to prepare the samples. Bi_2O_3, Na_2CO_3, $BaCO_3$, Sc_2O_3, and TiO_2 of purities 99.0%, 99.8%, 98.0%, 99.9%, and 99.0%, respectively, were used as raw materials. The required quantity of each powder was computed according to the corresponding chemical formula, and the raw material powders were weighed using an electronic balance with a precision of 0.1 mg. The weighed raw material powders were added to absolute ethanol and the resulting mixture was further poured into a ball mill jar which contained zirconia balls. Mechanical milling was performed for 24 h to ensure full and uniform mixing. The mixture of the raw material after ball grinding was then dried at 90 °C and further calcinated at 880 °C for 2 h. An appropriate amount of 7% polyvinyl alcohol (PVA) binder was added to the formula powder obtained after pre-sintering, and this was further followed by uniform mixing. The formula powder was dried and passed through a 100 mesh sieve to obtain granulated powder. The granulated powder was pressed into green bodies with a dimension of 13 mm and a thickness of 1 mm at 40 MPa. Subsequently, the PVA binder were released from green bodies at 600 °C, heated at 1150 °C for 2 h, and cooled inside the furnace to 30 °C. The sintered samples were polished and cleaned on both sides, and a silver paste with a diameter of 8 mm was printed and held at 600 °C for 30 min to obtain a silver electrode. After cooling to room temperature, the samples were taken out for electrical performance testing.

X-ray diffraction (XRD, Empyrean Pixcel3D) was used to analyze the phase structure of the ceramics, while field emission scanning electron microscopy (FESEM, Quanta 450 FEG, FEI) was used to observe the surface morphology and grain size of the samples. A computer-controlled impedance analyzer (4294A, Agilent) was used to determine the temperature-dependent dielectric properties from ambient temperature to 600 °C. An impedance analyzer (Agilent 4294) was used to measure the temperature-dependent impedance spectrum from 40 Hz to 1 MHz. The current–electric field (*I*–*E*) curves and polarization–electric field (*P*–*E*) hysteresis loops of the samples were measured by a ferroelectric tester (TF Analyzer 2000, aixACCT).

3 Results and discussion

The XRD patterns of the BNT–BS–xBT ceramics are shown in Fig. 1. The XRD patterns of all compositions have a single perovskite structure, which indicates the dissolution of BT into the 0.9BNT–0.1BS matrix to form a new solid solution. Figure 1b and c are the enlarged images of the (111) and (200) diffraction peaks, respectively.

As we known, pure BNT is rhombohedral phase and pure BT is tetrahedral phase [19]. Peak splitting of (111) peak

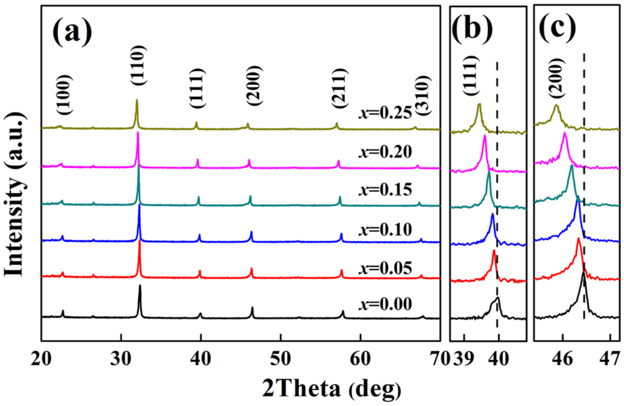

Fig. 1 **a** XRD patterns of BNT-BS-xBT ceramics; **b**, **c** the magnification of (111) and (200) peaks

at 40° implies that there is rhombohedral phase, and the splitting at 46.5° for (200) peak indicates the tetrahedral phase [20]. In Fig. 1b and c, all peaks have non-splitting peak characteristics, which suggests that the BNT–BS–*x*BT ceramics have pseudo-cubic structures. The related phenomena have been reported by Hiruma, in which the crystal structure of BNT–$KNbO_3$ and BNT–$NaNbO_3$ ceramics transforms from rhombohedral to pseudo-cubic indicating a ferroelectric transformed into antiferroelectric [21]. However, the (111) and (200) peaks are asymmetric due to the existence of shoulder peaks, which implies that the ceramics are not complete pseudo-cubic structure, that is the rhombohedral and tetrahedral phases don't completely transform into pseudo-cubic phase. It should be noted that the symmetry of (111) and (200) peaks increases gradually with the increase of BT content, which indicates that BT makes the phase structure of these ceramics transform into pseudo-cubic more thorough. Furthermore, it is observed that the (111) and (200) diffraction peaks shift to low angles with an increase in BT content. This shift can be ascribed to the crystal lattice expansion of the 0.9BNT–0.1BS ceramics. Such enlargement of the crystal lattice occurs because the ionic radius of Ba^{2+} is greater than that of the A-site and the ionic radius of Ti^{4+} is similar to that of the B-site in the 0.9BNT–0.1BS matrix.

Figure 2 shows the microscopic morphologies of the BNT–BS–*x*BT ceramics. The 0.9BNT–0.1BS ceramics have a compact and square structure. The average grain size of ceramics is 3.2 μm at $x=0$ in Fig. 3a. After doping BT component, the grain size of the BNT–BS–*x*BT ceramics gradually decreased. At $x=0.25$, shown in Fig. 3f, the average grain size is 1.71 μm and the grain shape changed from a cubic to spherical configuration along with a decrease in compactness. This may be due to the substitution of Na^+ ions by Ba^{2+} ions, which are similar in radii to Na^+ ions. When Ba^{2+} ions replace Na^+ ions, V_{Na}' is produced in the ceramics cell in order to maintain the balance of chemical valence, which decreases the ceramic density and further makes the lattice structure incompact [22].

Figure 4a shows the *P*–*E* hysteresis loops of the BNT–BS–*x*BT ceramics at an electric field lower than 70 kV/cm. The hysteresis loops of all samples have slender curves with small E_c and P_r, indicating that the BNT–BS–*x*BT ceramics possessed strong relaxor characteristics. With an increase in BT content (Fig. 4b), the maximum polarization (P_{max}) first increases and then decreases, but P_r does not show any variation. When $x=0.15$, the difference between P_{max} and P_r reaches a maximum value; this can be beneficial in obtaining good energy storage properties. The composition dependence of the W_{rec} and η of the BNT–BS–*x*BT ceramics is plotted in Fig. 4c. W_{rec} and η show a trend similar to that of P_{max} and P_r. When $x=0.20$, W_{rec} and η can reach the peak value of 0.563 J/cm^3 and 63%, respectively. The critical point of $x=0.15$ can be observed when the difference between P_{max} and P_r is becomes larger; however, this composition does not suggest that the energy storage density reaches a maximum value. As shown in Fig. 4d, P1 and P2 are polarization differences at $x=0.15$ and 0.20, respectively. Although the polarization difference at $x=0.15$ is greater than that at $x=0.20$, the *P*–*E* loops are much flatter at $x=0.2$ due to the BT component doping, which enhances the relaxor properties of the BNT–BS–*x*BT ceramics. The relaxor state is conducive for increasing the energy storage

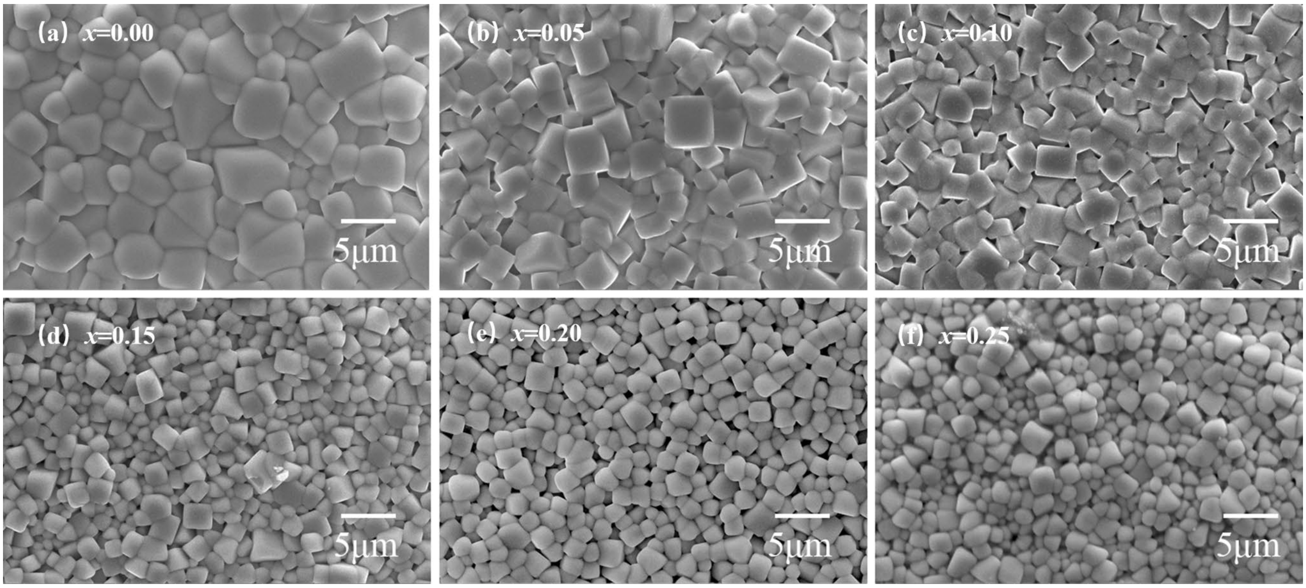

Fig. 2 Surface morphologies of BNT-BS-*x*BT ceramics

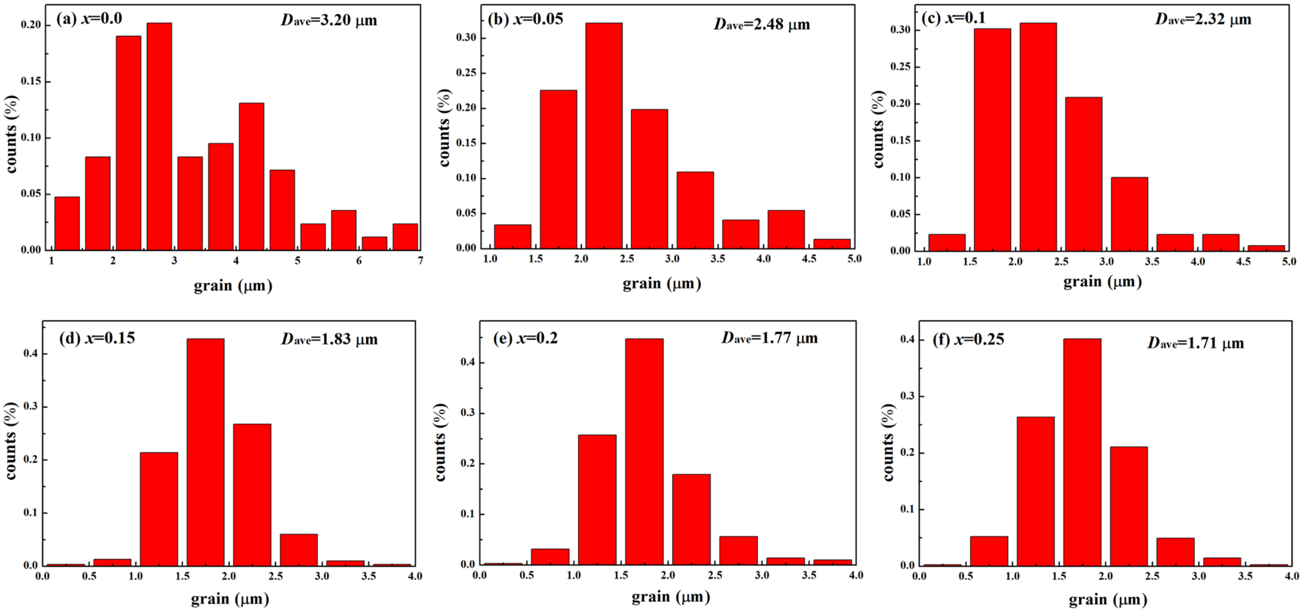

Fig. 3 Average grain size of BNT-BS-*x*BT ceramics

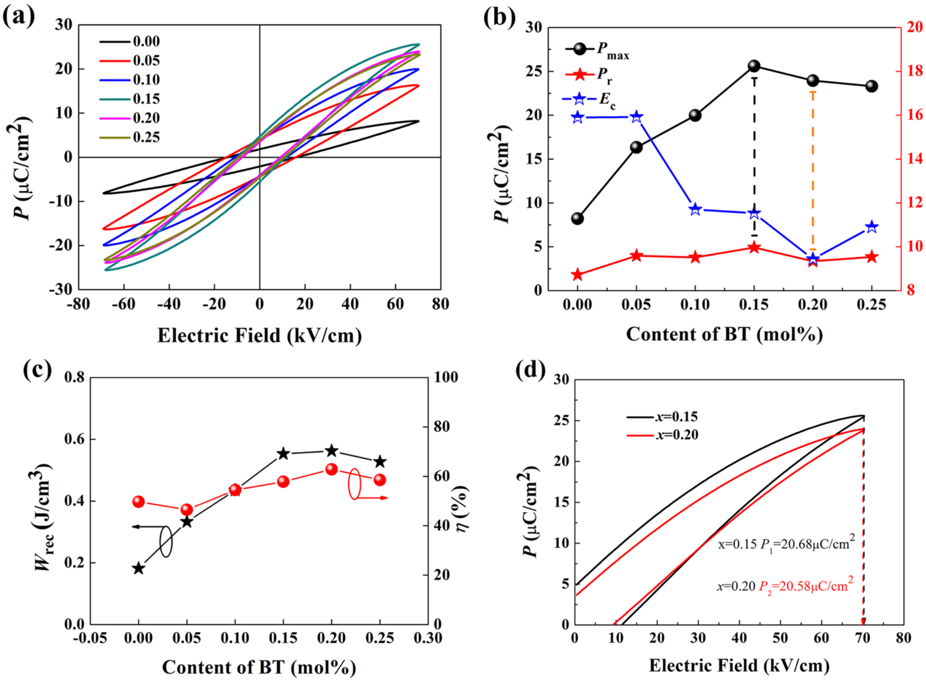

Fig. 4 **a** Hysteresis loops of BNT-BS-*x*BT ceramics, **b** variation trend of $P_{\max}$, P_r and E_c, **c** energy storage density and efficiency of BNT–BS–*x*BT ceramics; **d** unipolar hysteresis loops of BNT–BS–*x*BT ceramics ($x = 0.15$, 0.20)

density. Therefore, BT can improve the energy storage performance of BNT–BS matrix.

The relaxor characteristics of the BNT–BS–*x*BT ceramics were also reflected in the strain curves. Figure 5a shows the field-induced strain (*S*–*E*) curves of the BNT–BS–*x*BT ceramics at 70 kV/cm. Assuming that the BNT–BS–*x*BT ceramics are in an relaxor state, the *S*–*E* curves are shaped as a sprout without the negative strain, which indicates low ferroelectric domain movement [23–26]. With an increase in the BT content of the solid solution, the maximum field-induced strain gradually increased from 0.02 to 0.15% and began to appear slightly asymmetrical. BNT–BS–*x*BT ceramics are relaxor ferroelectrics with strong electrostriction behavior. Hence, the electrostriction coefficient (Q_{33}) was analyzed in this study. The S–P^2 curves can be linearly fitted according to the formula $S = Q_{33}\,P^2$, and the results are shown in Fig. 5c. The relationships between S and P^2 at all composition points are generally linear. Thus, the

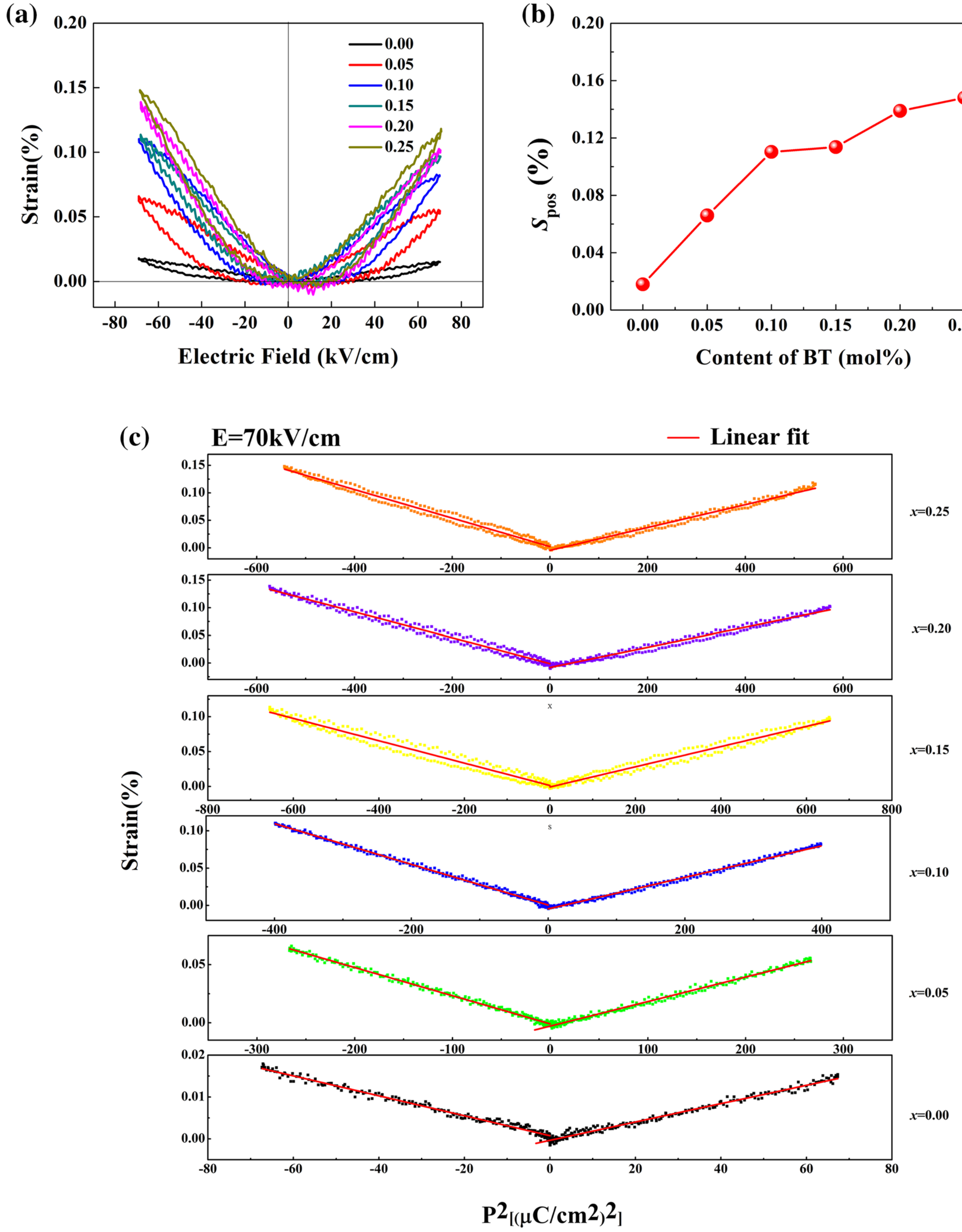

Fig. 5 **a** Strain curves of BNT–BS–*x*BT ceramics, **b** positive strain of BNT–BS–*x*BT ceramics, **c** linear fitting of *S*–P^2 curves

field-induced strain of the BNT–BS–*x*BT ceramics is mainly due to the electrostriction effect [27–29]. Table 1 shows the electrostriction coefficients (Q_{33}) of BNT–BS–*x*BT ceramics. Owing to the asymmetric strain of the ceramics, Q_{33} is calculated under positive and negative electric fields to derive the average value. When $x = 0.1$, the negative Q_{33} of the ceramics reaches the maximum value of 2.72325×10^{-2} m^4/C^2 with an average value of 2.41909×10^{-2} m^4/C^2. Compared with other BNT-based ceramics, for example, BNT–BT–KNN ceramics, obtained a high electrostrictive coefficient of 2.4×10^{-2} m^4/C^2 at an electric field of less than 60 kV/cm [30], the BNT–BS–*x*BT ceramics were not only able to withstand a higher electric field (70 kV/cm), but also had a higher electrostriction coefficient of

Table 1 Electrostriction coefficient Q_{33} in the negative, positive branches of S–P^2 curves and average Q_{33} for BNT-BT-xBT ceramics at 70 kV/cm

Composition	Q_{33} (m^4/C^2) ($E = 70$ kV/cm)		
	Negative branch	Positive branch	Average
$x = 0.00$	2.38299×10^{-2}	2.19493×10^{-2}	2.28896×10^{-2}
$x = 0.05$	2.42371×10^{-2}	2.11025×10^{-2}	2.26698×10^{-2}
$x = 0.10$	2.72325×10^{-2}	2.11092×10^{-2}	2.41909×10^{-2}
$x = 0.15$	1.60348×10^{-2}	1.44875×10^{-2}	1.52612×10^{-2}
$x = 0.20$	2.34405×10^{-2}	1.82174×10^{-2}	2.08290×10^{-2}
$x = 0.25$	2.58919×10^{-2}	2.07591×10^{-2}	2.18255×10^{-2}

2.72325×10^{-2} m^4/C^2. This may be attributed to the high electrostriction effect of the relaxor in the disordered state due to the large vibration space [31, 32].

Figure 6 shows the temperature dependence of the dielectric constant (ε_r) and dielectric loss (tanδ) of the BNT–BS–xBT ceramics at frequencies of 1, 10, and 100 kHz. As shown in Fig. 6a, the Curie temperature (T_m) of the ceramics is 372 ℃ at $x = 0$. The T_m peak shifts to the low-temperature region with an increase in the BT content of the solid solution. When $x = 0.25$ (Fig. 6f), the T_m peak decreases to 232 ℃, indicating that the increase in the BT content inhibited the ferroelectric stability of the 0.9BNT–0.1BS ceramics [33]. Moreover, the maximum dielectric constant (ε_r) of the ceramics was also affected by the BT content of the solid solution. In particular, the maximum

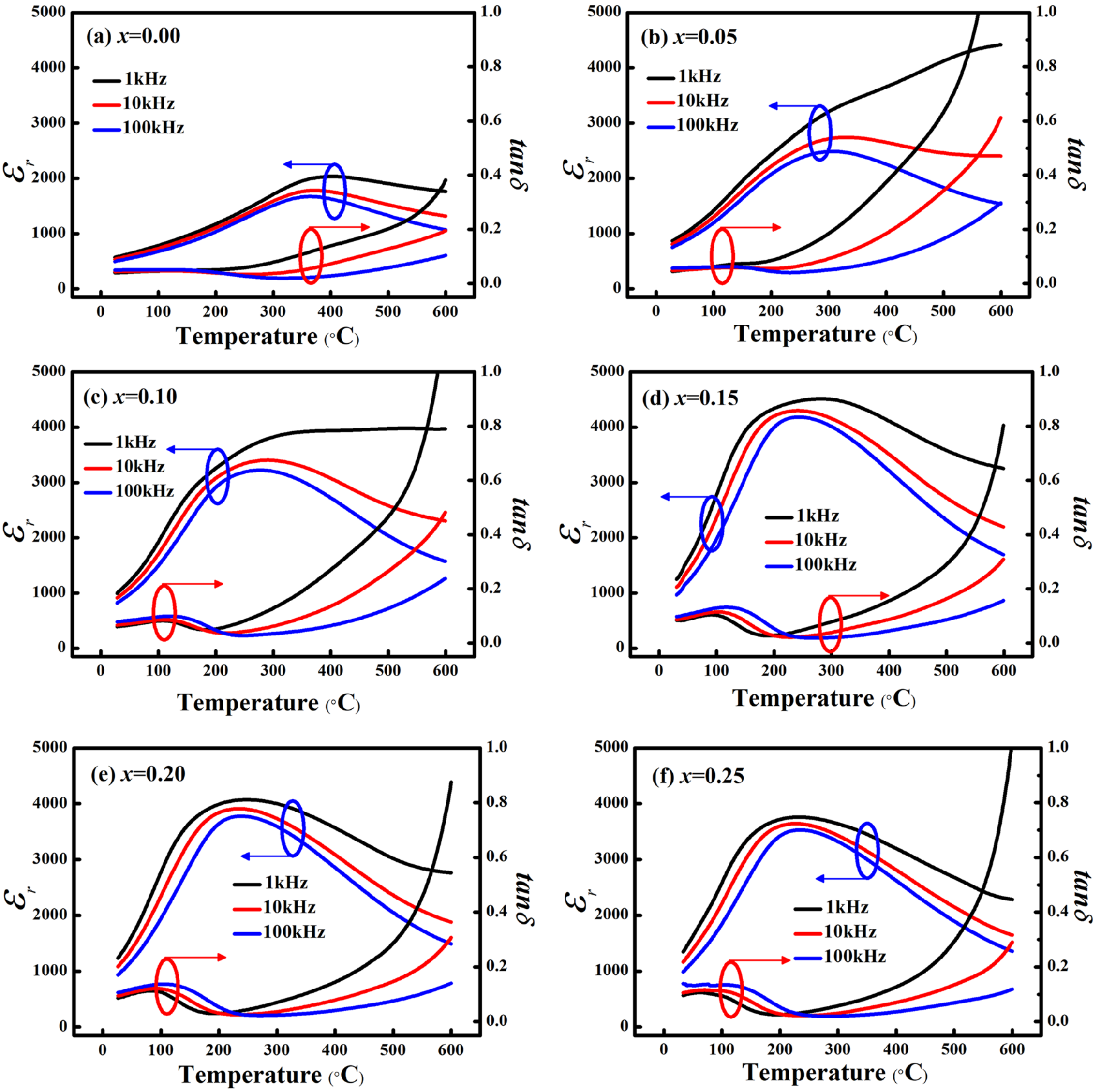

Fig. 6 Frequency and temperature dependence of the dielectric constant (ε_r) and dielectric loss (tanδ) of BNT–BS–xBT ceramics at the frequency of 1 kHz, 10 kHz, and 100 kHz

dielectric constant (ε_r) of the ceramics was 1670 at the test frequency of 100 kHz at $x = 0$. With the introduction of BT, the maximum dielectric constant (ε_r) of the ceramics increased significantly. When $x = 0.15$, the maximum dielectric constant (ε_r) reached the maximum value of 4185. Although the BT content continued to increase, the maximum dielectric constant (ε_r) of the ceramics remained stable at approximately 4000. Oxygen vacancies and ionic polarizability can be used to analyze the increase of dielectric constant [34]. As the ionic radius of Ba^{2+} (0.135 nm) is closer to that of Bi^{3+} (0.103 nm) than that of Na^{+} (0.102 nm), Ba^{2+} ions mainly replace Bi^{3+} ions. The substitution process generates oxygen vacancies inside the ceramics. The Ti element in BNT-based ceramics will transform from Ti^{4+} to Ti^{3+} during sintering process, which produces the oxygen vacancies [35–37]. The oxygen vacancies inside the ceramic cause the distortion of ceramic grain cells and an increase in the active area of Ti^{4+} within the Ti–O_6 octahedron; further, all such changes are beneficial to the relative displacement of the positive and negative ions inside the ceramic at 90° domain steering [34]. The ionic polarizability of Ba^{2+} ion is 1.31 C m^2/V, which is larger than that of Na^{+} (0.199 C m^2/V) and Bi^{3+} (0.387 C m^2/V), Ba^{2+} ions are easier to be polarized than Bi^{3+} and Na^{+} ions [34, 38]. Hence, the dielectric constant of BNT–BS–*x*BT ceramics is increased because of the above two reasons. Moreover, the dielectric loss (tanδ) of the ceramics increased sharply at high temperatures due to the introduction of BT in the solid solution, which may be related to the polarization of the space charge within the ceramics by the Shockley–Read mechanism [39, 40]. At the same time, the dielectric coat temperatures less thnstant (ε_r) of the ceramics depended largely on frequency. When the temperature was lower than T_m, the frequency dispersion decreased; however, when the temperature became higher than T_m, the frequency dispersion increased. This phenomenon is due to the change in symmetry of the polar nanoregions (PNRs) within the ceramics and the relaxation of these PNRs at high temperatures [41]. The BNT–BS–*x*BT ceramics are relaxor ferroelectrics.

Figure 7a shows the impedance spectrum of the BNT–BS–0.2BT ceramic from 100 to 550 °C (40 Hz–1 MHz). Only single semi-circular arc is observed for the impedance spectrum at different temperatures in the test frequency range. The semi-circular arc of the BNT–BS–0.2BT ceramics is essentially a Debye-like semicircle without distortion, and its impedance behavior can be derived from the internal grain effect of the material. The impedance spectra show strong linear characteristics at temperatures less than 450 °C, and a complete semicircle appears gradually when the temperature increases to 500 °C, which indicates that the ceramic material has good insulation properties [42]. Figure 7b shows the relationship between the imaginary part of the impedance spectra ($-Z''$) and the frequency (f) of the BNT–BS–0.2BT ceramics. Only one characteristic peak at different test temperatures can be observed, which corresponds to the semicircle in the temperature range of 450–550 °C in the impedance spectra. The grains of the BNT–BS–0.2BT ceramic are ferroelectric, and the grain boundary is amorphous and non-ferroelectric. Thus, the grains of the BNT–BS–0.2BT ceramic play a major role in the impedance of these materials. With an increase in temperature, the maximum value of the imaginary part of impedance decreased, which indicated that the BNT–BS–0.2BT ceramics had negative temperature coefficient characteristics [43]. Meanwhile, the characteristic peak shifted to the high-temperature region, indicating the extension of the relaxation time of polarizable grains and the existence of heat-induced relaxation in the ceramics [44–46].

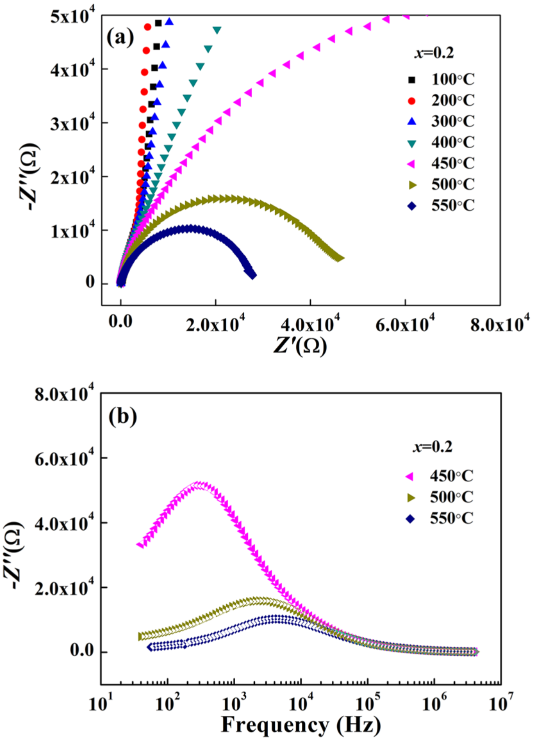

Fig. 7 **a** Impedance spectrum of BNT–BS–0.2BT ceramics, **b** the curve of $-Z''$ of BNT–BS–0.2BT ceramics at different frequencies in the temperature range of 450–550 ℃

4 Conclusion

The structure, ferroelectricity, strain, energy storage, dielectric, and impedance properties of 0.9BNT–0.1BS ceramics were significantly affected by doping BT. XRD shows that the phase structure is pseudo-cubic. The BT results in the lattice expansion, inhibits the grain growth, and increases the porosity of these ceramics. The average grain size is

3.2 μm at $x = 0$ and decreases gradually to 1.71 μm. The ceramic at $x = 0.20$ has a high η of 63%, and its W_{rec} reaches 0.563 J/cm^3. The field-induced strain increases with the increase in BT content. The strain obtains the maximum value of 0.15% at $x = 0.25$, and a high electrostriction coefficient of 2.72325×10^{-2} m^4/C^2 is achieved at $x = 0.10$. The T_m peaks decreases from 372 to 232 °C with the increase of BT content, indicating the decreasing of the ferroelectric stability. The maximum permittivity increases first and then decreases and reaches max value of 4185 at $x = 0.15$. The ceramics have good insulation properties, and the impedance behavior can be derived from the internal grain effect.

Acknowledgements This work is supported by the National Nature Science Foundation of China (Grant Nos. 11664006, 61965007), Guangxi Nature Science Foundation (Grant No. 2018GXNSFDA281042), and Guangxi Key Laboratory of Information Materials (Grant No. 171009-Z).

References

1. T.D. Zhang, W.L. Li, Y. Zhao, Y. Yu, W.D. Fei, Adv. Funct. Mater. **28**, 1706211 (2018)
2. V.D.N. Tran, T.H. Dinh, H.-S. Han, W. Jo, J.-S. Lee, Ceram. Int. **39**, S119 (2013)
3. X. Wang, L.W. Chan, C.L. Choy, Solid State Commun. **125**, 395 (2003)
4. W. Li, Z.J. Xu, R.Q. Chu, P. Fu, G.Z. Zang, J. Am. Ceram. Soc. **93**, 2942 (2010)
5. X.Y. Zhao, H. Wang, C.L. Yuan, J.W. Xu, Y.R. Cui, J.F. Ma, J. Mater. Sci. - Mater. Electron. **24**, 1480 (2013)
6. H. Wang, X.Y. Zhao, J.W. Xu, L. Yang, J. Mater. Sci. Electron. **26**, 6129 (2015)
7. H. Wang, X.Y. Zhao, J.W. Xu, X. Zhai, L. Yang, J. Mater. Sci. Mater. Electron. **27**, 2036 (2016)
8. W.J. Wu, D.Q. Xiao, J.G. Wu, J. Li, W.F. Liang, C. Zhang, Z. Wang, Z.Y. Li, J.G. Zhu, J. Funct. Mater. **11**, 2050 (2011)
9. M. Chandrasekhar, P. Kumar, Ceram. Int. **41**, 5574 (2015)
10. T. Takenaka, K. Maruyama, K. Sakata, Jpn. J. Appl. Phys. **30**, 2236 (1991)
11. H.P. Liu, X.Y. Huang, C.H. Gao, Chin. Ceram. Soc. **24**, 70 (2005)
12. D. Li, Y. Lin, M. Zhang, H.B. Yang, Chem. Eng. J. **S1385**, 33144 (2019)
13. H.B. Yang, P.F. Liu, F. Yan, Y. Lin, T. Wang, J. Alloys Compd. **S0925**, 33500 (2018)
14. X.Y. Liu, H.B. Yang, F. Yan, Y. Qin, Y. Lin, T. Wang, J. Alloys compd. **778**, 97 (2019)
15. Y. Lin, D. Li, M. Zhang, H.B. Yang, J. Mater. Chem. C. https://doi.org/10.1039/c9tc06218a (2020)
16. S.T. Zhang, A.B. Kounga, W. Jo, C. Jamin, K. Seifert, T. Granzow, J. Rodel, D. Damjanovic, Adv. Mater. **21**, 4716 (2009)
17. S.T. Zhang, F. Yan, B. Yang, W.W. Cao, Appl. Phys. Lett. **97**, 122901 (2010)
18. F.F. Wang, C.C. Jin, Q.R. Yao, W.Z. Shi, J. Appl. Phys. **114**, 027004 (2013)
19. C.G. Xu, D.M. Lin, K.W. Kwok, Soild. State. Sci. **10**, 934 (2008)
20. Q. Xu, T.M. Li, H. Hao, S.J. Zhang, Z.J. Wang, M.H. Cao, Z.H. Yao, H.X. Liu, J. Eur. Ceram. Soc. **35**, 545 (2015)
21. Y. Hiruma, H. Nagata, T. Takenaka, J. Appl. Phys. **104**, 124106 (2008)
22. Y. Qu, D. Shan, J. Song, Mater. Sci. Eng. B **121**, 148 (2005)
23. W.G. Ma, Y.W. Zhu, M.A. Marwat, P.Y. Fan, B. Xie, D. Salamon, Z.G. Ye, H.B. Zhang, J. Mater. Chem. C **7**, 281 (2019)
24. D.S. Yin, Z.H. Zhao, Y.J. Dai, Z. Zhao, X.W. Zhang, S.H. Wang, J. Am. Ceram. Soc. **99**, 2354 (2016)
25. N. Kumar, T.Y. Ansell, D.P. Cann, J. Appl. Phys. **115**, 154104 (2014)
26. M.L. Liu, D.A. Yang, Y.F. Qu, J. Alloys Compd. **496**, 449 (2010)
27. S.J. Pang, L. Yang, J.Y. Qin, H. Qin, H. Xie, H. Wang, C.R. Zhou, J.W. Xu, Appl. Phys. A **125**, 119 (2019)
28. S. Nomura, K. Uchino, Ferroelectrics **41**, 117 (1982)
29. J.G. Hao, Z.J. Xu, R.Q. Chu, W. Li, J. Du, J. Mater. Sci. **50**, 5328 (2015)
30. J.G. Hao, C.G. Ye, B. Shen, J.W. Zhai, J. Appl. Phys. **114**, 054101 (2013)
31. L. Jin, R.J. Huo, R.P. Guo, F. Li, D.W. Wang, Y. Tian, Q.Y. Hu, X.Y. Wei, Z.B. He, Y. Yan, G. Liu, ACS Appl. Mater. Interfaces. **8**, 31109 (1944)
32. S.T. Zhang, A.B. Kounga, W. Jo, C. Jamin, K. Seifert, T. Granzow, R. Jürgen, D. Damjanovic, Adv. Mater. **21**, 4716 (2009)
33. C. Wang, X.J. Lou, T.D. Xia, S.T. Tian, Ceram. Int. **43**, 9253 (2017)
34. W.F. Mu, H.L. Du, X. Shi, S.M. Du, J. Chin. Ceram. Soc. **39**, 1941 (2011)
35. W.B. Hu, Y. Liu, R.L. Withers, T.J. Frankcombe, L. Noren, A. Snashall, M. Kitchin, P. Smith, B. Gong, H. Chen, J. Schiemer, F. Brink, W.-L. Jennifer, Nat. Mater. **12**, 821 (2013)
36. W. Dong, W.B. Hu, T.J. Frankcombe, D.H. Chen, C. Zhou, Z.X. Fu, C. Ladir, G.Q. Hai, H. Chen, Y.X. Li, R.L. Withers, Y. Liu, J. Mater. Chem. A **5**, 5436 (2017)
37. Z.T. Li, H. Liu, H.C. Thong, Z. Xu, M.H. Zhang, J. Yin, J.F. Li, K. Wang, J. Chen, Adv. Electron. Mater. **5**, 1800756 (2018)
38. Y.B. Feng, S.Y. Zhang, H.T. Sun, Y. Li, Y.Y. Zhu, J. Dalian Inst. Light Ind. **19**, 98 (2000)
39. R.R. Neurgaonkar, J.R. Oliver, W.K. Cory, L.E. Cross, Mater. Res. Bull. **18**, 735 (1983)
40. R.R. Neurgaonkar, J.G. Nelson, J.R. Oliver, L.E. Cross, Mater. Res. Bull. **25**, 959 (1990)
41. C. Jiang, X.F. Zhou, K.C. Zhou, C. Chen, H. Luo, X. Yuan, D. Zhang, J. Eur. Ceram. Soc. **36**, 1377 (2016)
42. J.R. Cheng, G.Y. Shi, Y.F. Qi, J.G. Chen, Y.S. Wen, J. Shanghai Univ. (Natural Science Edition) **17**, 213 (2011)
43. G.B. Liu, H. Wang, H. Xie, S.J. Pang, C.R. Zhou, J.W. Xu, J. Inorg. Mater. **33**, 1331 (2018)
44. G.C. Liu, H.Q. Fan, G.Z. Dong, J. Shi, Q. Chang, J. Alloys Compd. **664**, 632 (2016)
45. S.N. Das, A. Pattanaik, S. Kadambini, S. Pradhan, S. Bhuyan, R.N.P. Choudhary, J. Mater. Sci. Mater. Electron. **27**, 10099 (2016)
46. M.A. Rafiq, M. Rasheed, Q.K. Muhammad, M. Waqar, M. Zubair, J. Mater. Sci. Mater. Electron. **28**, 15009 (2017)